

(計畫名稱)

基於光子晶體微共振腔之高靈敏光感測器元件之研究

計畫類別： 個別型計畫 整合型計畫

計畫編號：98-2221-E-009-015-MY2

執行期間：98 年 8 月 1 日至 100 年 7 月 31 日

計畫主持人：李柏璵 副教授

共同主持人：

計畫參與人員：盧贊文，林品佐，蔡家揚，蕭君源，邱立勳，呂紹平

成果報告類型(依經費核定清單規定繳交)： 精簡報告 完整報告

本成果報告包括以下應繳交之附件：

赴國外出差或研習心得報告一份

赴大陸地區出差或研習心得報告一份

出席國際學術會議心得報告及發表之論文各一份

國際合作研究計畫國外研究報告書一份

處理方式：除產學合作研究計畫、提升產業技術及人才培育研究計畫、
列管計畫及下列情形者外，得立即公開查詢

涉及專利或其他智慧財產權， 一年 二年後可公開查詢

執行單位：國立交通大學光電工程學系

摘要：

在這份報告中，我們呈現了從 2009 年 8 月到 2011 年 7 月間，本計畫執行之完整研究成果。本計畫的主要研究課題著重於以二維光子晶體微/奈米共振腔，實現具有高共振腔 Q 值、高感測靈敏度以及具有可整合於積體晶片之元件尺寸的光學折射率、生物尺寸粒子與應力感測器。為了實現上述目的，透過完整的數值模擬、三五族半導體製程以及奈米光電量測系統，我們以半導體雷射的形式驗證並實現了具有高 Q 模態、且對環境變化敏感的新穎光子晶體共振腔。包括了：(1) 具有表面波模態之光子晶體板緣共振腔，(2) 正方光子晶體晶格 D_0 超小奈米共振腔，(3) 多功能二維蜂巢狀光子晶體薄板，(4) 對應力敏感之雙層光子晶體共振腔。

而透過設計相關的氣體、液體待測物測試平台以及發展有機 (蛋白質) /無機 (三五族半導體) 材料介面接合的後製程，我們利用上述元件在模擬與實驗上實現了一連串高靈敏度光學感測，包括：(1) 具有最小可偵測折射率變化 3.5×10^{-4} 的氣體與液體感測，(2) 最小可偵測重量 0.8 fg 的蛋白質吸附感測，(3) 一種基於模態極化變化的非光譜式奈米顆粒感測機制，以及 (4) 最小可偵測的應力變化 0.95 奈牛頓。基於上述所達成的光學感測雛形，本研究計畫中所提之光子晶體共振腔確實具有極大的潛力與可能性得以實現高靈敏度的積體光學感測晶片。

關鍵詞：光子晶體，微/奈米共振腔，半導體雷射，光學感測器

Abstract

The research results during the project period from August, 2009 to July, 2011 are presented in this report. The main research topics of this project are focused on novel two-dimensional (2D) photonic crystal (*PhC*) micro- and nano-cavities with high quality (*Q*) factors for realizing highly sensitive optical index, bio-sized nano-particle, and stress sensors, which can be integrated on micro-scale bio-chips. To reach these goals, a variety of numerical simulations, well-developed III-V semiconductor nano-fabrication processes, and various nano-opto-electronic measurement systems are utilized, which allow us to design and demonstrate various novel *PhC* cavities with high *Q* modes sensitive to the environmental variations, including: (1) *PhC* slab-edge microcavities with surface modes, (2) ultra-small square-*PhC* D_0 nanocavity, (3) multi-functional 2D honeycomb *PhC* slabs, and (4) double-layered *PhC* microcavities with stress-sensitive defect modes.

Via designing gas and liquid analyte platforms and developing post-fabrication process for forming the linking layer at the organic (protein) / in-organic (III-V semiconductor material) interface, highly sensitive optical sensing is achieved via above *PhC* devices, including: (1) the minimum detectable index variation of 3.5×10^{-4} for gas and liquid analytes, (2) the minimum detectable mass of 0.8 fg for protein adsorption, (3) a spectral-free approach for detecting single bio-sized nano-particle (~ 350 nm in diameter) based on polarization variation, and (4) the minimum detectable applied stress of 0.95 nN. According to the demonstrated prototypes of optical sensors in this project, the proposed *PhC* micro- and nano-cavities show strong possibilities in realizing highly sensitive optical sensors on-chip.

Keywords : photonic crystal, micro- and nano-cavities, semiconductor lasers, optical sensors

Content

Goals of this Project

Achievements and Discussions

- I. Surface Modes in *PhC* Slab-Edge Microcavities
 - (I) High Q Surface Mode Lasing from *PhC* Hetero-Slab-Edge Microcavities
 - (II) High Index Sensitivity of the Surface Mode via Gas Sensing
 - (III) Summary

- II. *SPhC* Point-Shifted D_0 Nanocavity for Protein and Single Nano-Particle Detection
 - (I) Nanocavity Design and Modal Properties
 - (II) Post-Fabrication Process for Forming the Linking Layer at In-Organic / Organic Interface
 - (III) Protein Adsorption Detection
 - (IV) Spectrum-Free Detection of Nano-Particle
 - (V) Summary

- III. Multi-Functional Two-Dimensional Honeycomb *PhC* Slab
 - (I) Band-Edge Modes near Γ Point in 2D Honeycomb *PhC* Slab
 - (II) Applications for Lasers, Optical Sensors, and High Brightness Light Emitters
 - (III) Summary

- IV. Double-Layered *PhC* Microcavities for Optically Sensing Stress
 - (I) Design Principles of Double-Layered *PhC* Microcavities
 - (II) Modal Properties for Stress Sensing
 - (III) Summary

Conclusions

Publications during the Project Period (2009 - 2011)

Goals of this Project

This project is focused on developing novel two-dimensional (2D) photonic crystal (*PhC*) micro- and nano-cavities to realize highly sensitive optical index, bio-sized nano-particle, and stress sensors. Owing to the condensed size of *PhC* cavities, we expect the sensors can be with high sensitivity, small device sizes, and feasible for integrated bio-chip. To achieve these goals, two essentials have to be fulfilled:

- 1. High Quality (*Q*) Modes in *PhC* Cavities for Sufficiently High Spectral Resolution**
- 2. High Sensitivity to the Environmental Fluctuations**

To fulfill these essentials, in this project, we have designed and realized several novel *PhC* cavities via the form of semiconductor lasers, including:

- 1. *PhC* Slab-Edge Microcavities with Surface Modes**
- 2. Double-Layered *PhC* Microcavities with Displacement-Sensitive Defect Modes**
- 3. *PhC* Nanocavity with High *Q* Whispering-Gallery Mode**
- 4. 2D Honeycomb *PhC* Slab with Band-Edge Modes near Γ Point**

Via these *PhC* cavities, optically sensing index variation, protein adsorption, single bio-sized nano-particle, and stress variation are demonstrated. The detailed descriptions of our achievements are provided in the following sections.

Achievements and Discussions

I. SURFACE MODES in *PhC* SLAB-EDGE MICROCAVITIES

Very recently, index sensors based on *PhC* defect micro- and nano-cavities have been demonstrated and optimized theoretically, which show the abilities of sensing very small index variation or nano-particles attachments within very condensed volume. However, most of the recent reports are based on defect modes confined in the cavities (dielectric region), which limit the sensing performance, for example, sensing response R_n , minimum detectable index or mass variation, and so on. Intuitively, the surface wave would be a very good candidate for a highly-sensitive optical sensor because the mode field extends into the environments.

(I) High Q Surface Mode Lasing from *PhC* Hetero-Slab-Edge Microcavities

Generally, the surface wave appears at the interface between metal with attenuation coefficient and dielectric material. However, in a 2D truncated *PhC* slab shown in Fig. 1(a), the surface wave will form and propagate along the interface between the dielectric *PhC* slab and air due to the total-internal reflection (TIR) and photonic band gap (PBG) effects. The simulated electric field distribution of the surface wave and the definition of slab-edge termination parameter τ are both shown in Fig. 1(b).

To well confine this surface wave in a slab-edge segment with finite length, taking a 2D hexagonal-*PhC* (HPhC) slab for example, two different *PhC* slab-edges H_1 and H_2 are used to form a reflection interface (mirror) by mode gap effect, as shown in Fig. 1(c). For a given H_1 slab-edge, the H_2 slab-edge is obtained by shrinking and shifting the air holes at the slab-edge of H_1 . In the band diagram shown in Fig. 1(d), the allowed surface mode frequency in H_2 will shift to be lower than that in H_1 . And the mode gap denoted by a shadow region in Fig. 1(d) will form due to this frequency difference between H_1 and H_2 . Thus, the surface mode in H_1 with frequency inside the mode gap cannot propagate in H_2 and H_2 can serve as a mirror.

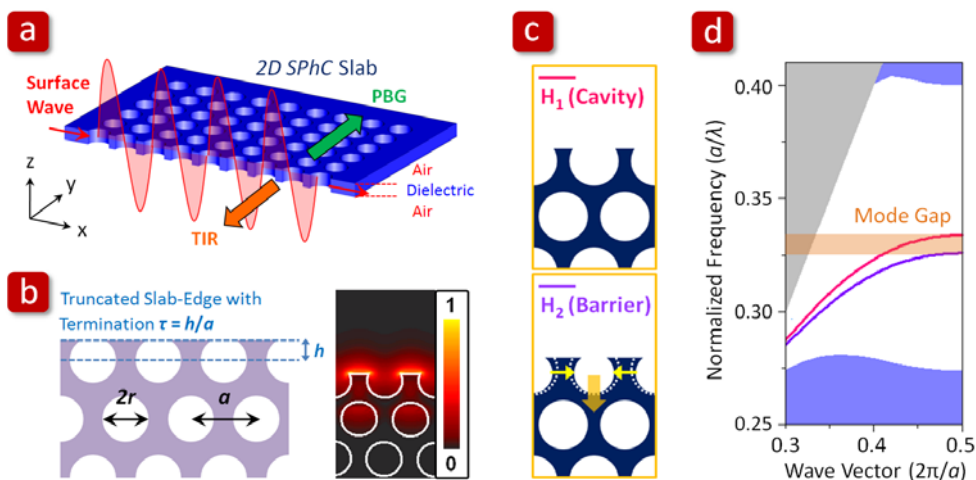


Fig. 1: (a) Scheme of surface mode propagating along the 2D truncated *PhC* slab surrounded by air. (b) The definition of slab-edge termination parameter τ and the simulated electric field of the surface wave propagating along the slab-edge. (c) Two different HPhC slab-edges H_1 , H_2 , and (d) the calculated dispersion curves of these two slab-edges.

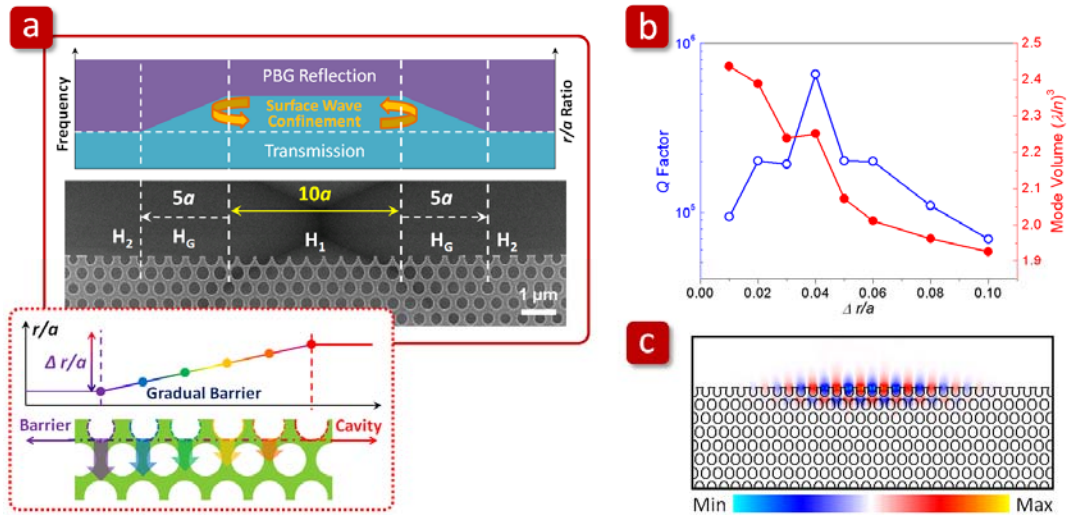


Fig. 2: (a) Scheme and SEM picture of HPhC HSE microcavity with cavity (H_1), gradually-varying barrier (H_G), and outer barrier (H_2) layers. The r/a ratio distribution and the formed mode gap in frequency by these three regions are also illustrated in the inset. (b) The simulated Q and V versus $\Delta r/a$. (c) The simulated surface mode profile in electrical field in x - y plane when $L = 10a$, $H_G = 5a$, and $\Delta r/a = 0.04$.

By applying double hetero-interfaces mentioned above, we design a HPhC hetero-slab-edge (HSE) microcavity, as shown by the scheme and scanning electron microscope (SEM) picture in Fig. 2(a). The surface mode in microcavity region with slab-edge H_1 will be confined in a frequency well via mode gap effect provided by the gradually-varying and outer barriers with slab-edges H_G and H_2 . For H_G , the radii and positions of air holes at the slab-edge are shrunk and shifted gradually and linearly, as shown in the inset of Fig. 2(a). The air-hole radius (r) over lattice constant (a) (r/a) ratios of the remaining outer barrier H_2 are kept invariant, and the r/a ratio difference between H_1 and H_2 is denoted as $\Delta r/a$. By three-dimensional (3D) finite-difference time-domain (FDTD) simulations, we optimize the Q factor of surface mode in HPhC HSE microcavity. An optimized high Q factor of 6.6×10^5 is obtained when $L = 10a$, $H_G = 5a$, and $\Delta r/a = 0.04$, as shown in Fig. 2(b). The simulated surface mode profile in electrical field in x - y plane is shown in Fig. 2(c). From Fig. 2(c), we can see the significant electrical field concentrations in the air region, which implies high sensitivity of this surface mode to the environmental index variation.

In fabrication, the epitaxial structure consisted of four 10 nm compressively strained *InGaAsP* multi-quantum-wells (MQWs) with 220 nm thickness is prepared. The measured photoluminescence (PL) is centered at 1530 nm. The MQWs is deposited a silicon nitride hard mask and spin-coated electron-beam (e-beam) resist in sequence. The PhC patterns are defined by electron-beam lithography on the resist layer. After a series of reactive ion etching and inductively coupled plasma etching, the PhC slab is formed by HCl selective wet-etching process.

The devices are optically pumped by a pulsed diode laser with 20 ns pulse width at room temperature. The typical light-in light-out (L - L) curve is shown in Fig. 3(a) and the threshold is estimated to be 0.55 mW at pump position A. The lasing spectrum near 1550 nm is shown in Fig. 3(b) by curve A. The measured spectral line width near threshold is estimated to be 0.24 nm by Lorentzian fitting as shown by the inset of Fig. 3(a), which corresponds to a Q factor of 6,400. To further confirm surface mode localization in the HSE microcavity, the pump position is moved outside the microcavity to positions B, C, and D, and no lasing action is observed as shown in Fig. 3(b).

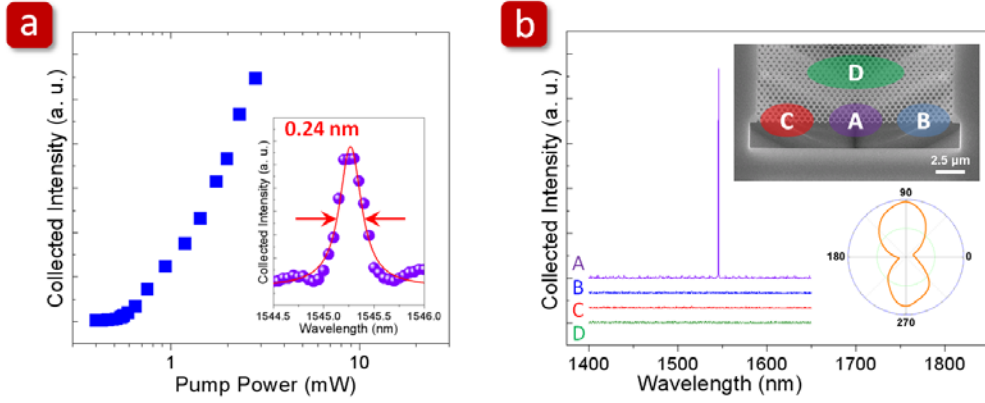


Fig. 3: (a) L - L curve and (b) lasing spectrum (curve A) near 1550 nm when pumping the cavity region (position A) and spectra (curves B, C, and D) when pumping outside the cavity region (positions B, C, and D). Spectrum near threshold with Lorentzian fitting and polarization of the surface mode are shown as the insets of (a) and (b).

In addition to $HPhC$, we also apply the similar HSE microcavity design on a square- PhC ($SPhC$) slab. Even though the $SPhC$ has weaker PBG effect than that of the $HPhC$, we show that high Q surface modes can be created in a $SPhC$ slab-edge based on our proposed mode gap confinement mechanism. We investigate and optimize different surface modes in $SPhC$ HSE microcavities with reduced cavity sizes and different slab-edge termination parameters τ both in simulations and experiments, which provide a guideline for achieving high Q and low threshold surface mode lasing. The $SPhC$ HSE microcavity design is similar to that of $HPhC$ shown in Fig. 2(a). The initial parameters are as follows: (1) The r/a ratio and length of the cavity H_1 are 0.38 and $6a$. (2) The $\Delta r/a$ ratio is chosen as 0.03. (3) The length of gradual mirror H_G is $5a$.

According to above parameters, we vary the τ of cavity H_1 from 0 to 0.90. By 3D $FDTD$ simulations, we find three high Q surface modes under different τ , which are denoted as the DD_{1-} , DD_{2-} , and DD_{3-} -modes. The surface modes we investigate here are all 0^{th} -order fundamental modes. The first and second letters stand for the mode behaviors in the air and PhC regions, respectively. We use the letters D and E to mean *Decay* and *Extended*. Among these modes, the DD_{3-} -mode lies inside the 2^{nd} - PBG of the $SPhC$, which has high Q factor of 9.1×10^4 and small mode volume (V) of $0.117 \mu\text{m}^3$ when $\tau = 0.80$, as shown in Fig. 4(a). These lead to a high Q/V value and are beneficial for laser source in quantum electro dynamic devices and photonic integrated circuits ($PICs$). With the fixed τ of 0.80, we further optimize the Q factor of the DD_{3-} -mode in HSE microcavity by varying $\Delta r/a$ from 0.02 to 0.18. The simulated Q and V under different $\Delta r/a$ are shown in Fig. 4(b). When $\Delta r/a = 0.09$, we obtain a high Q factor of 2.3×10^5 and a small V of $0.105 \mu\text{m}^3$ (close to one wavelength cubic). The simulated electric field components (E_x and E_y) of the DD_{3-} -mode are shown in Fig. 4(c).

In fabrication, designing the patterns with proper proximity corrections for e -beam lithography is very important, which assures that we can fabricate the optimized τ and $\Delta r/a$ ratio obtained in simulation, and keep the r/a ratio uniform near the slab-edge of the fabricated devices. SEM pictures of the fabricated slab-edges with $\tau = 0$ to 0.90, top-, and tilted-view SEM pictures of the $SPhC$ HSE microcavity are shown in Figs. 5(a) - (c). From the zoom-in SEM pictures of cavity H_1 , gradual mirror H_G , and outer mirror H_2 shown in Fig. 5(d), the fabricated a , τ , r/a and $\Delta r/a$ ratios are estimated to be 520 nm, 0.40, 0.38, and 0.02.

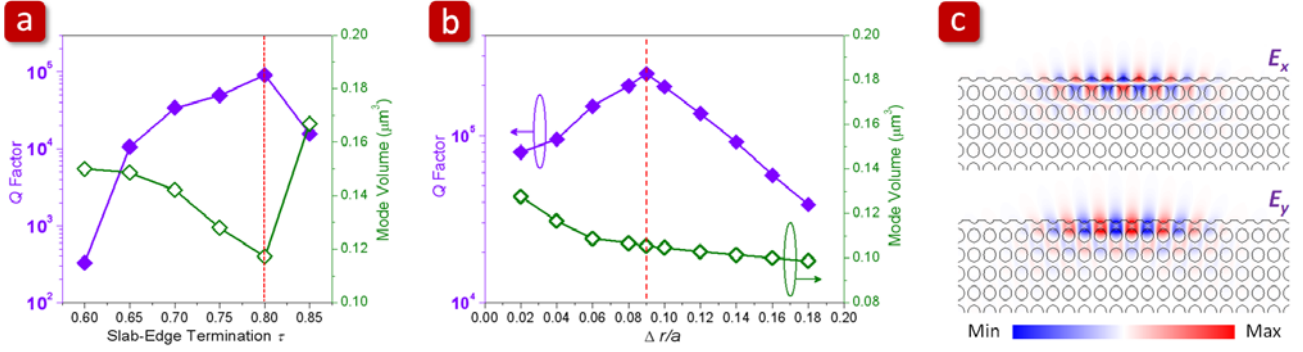


Fig. 4: (a) The simulated Q and V of the 0^{th} -order DD_3 -mode under different τ and fixed $\Delta r/a$ of 0.03. (b) The simulated Q and V of the DD_3 -mode under fixed τ of 0.80 and different $\Delta r/a$ from 0.02 to 0.18. (c) The simulated E_x - and E_y -fields of the DD_3 -mode in microcavity with $\tau = 0.80$ and $\Delta r/a = 0.09$.

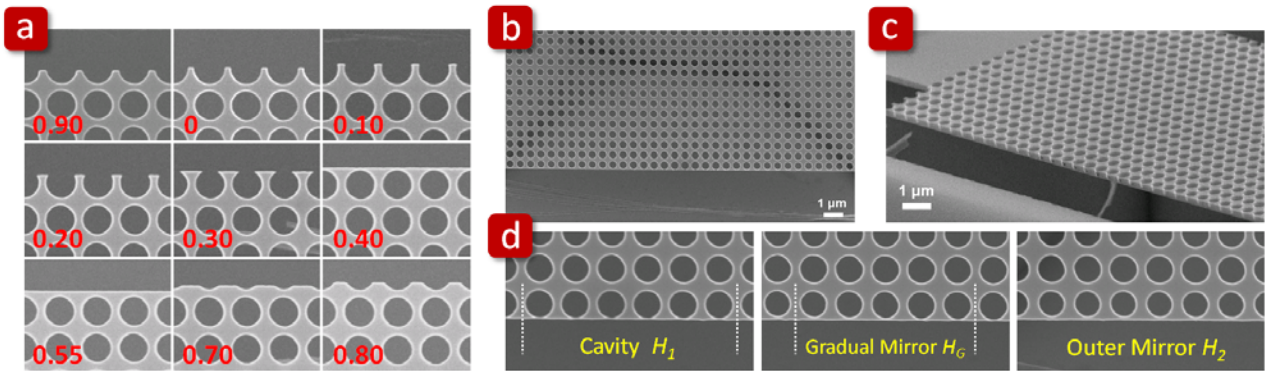


Fig. 5: (a) SEM pictures of the fabricated slab-edges with different τ from 0 to 0.90. (b) Top- and (c) tilted-view SEM pictures of the SPHC HSE microcavity with $\tau = 0.40$. (d) The zoom-in SEM pictures of cavity H_1 , gradual mirror H_g , and outer mirror H_2 , which show the well-controlled $\Delta r/a$ of 0.02.

According to the optimized results in simulation, the SPHC HSE microcavity with fabricated $a = 620 \text{ nm}$, $r/a = 0.38$, $\Delta r/a = 0.09$, and $\tau = 0.80$ shown as the insets in Fig. 6(a) is optically pumped at room temperature. The measured L - L curve and lasing spectrum in dB scale at 1556 nm are shown in Figs. 6(a) and (b), which show a very low threshold of $140 \mu\text{W}$ and side-mode suppression-ratio (SMSR) larger than 25 dB. The spectrum at 0.7 times threshold shown as the inset of Fig. 6(b) shows the measured line width of 0.28 nm, which corresponds to a high estimated Q factor of 5,500. The localization property of surface mode in HSE microcavity can be easily confirmed by moving the excitation laser spot from microcavity to SPHC and outer mirror regions, respectively, and no lasing action is observed when pumping these regions. To further confirm the surface mode lasing, lasing spectra of the DD_3 -mode at different τ from 0.70 to 0.85 are obtained and shown in the top of Fig. 6(c). The measured normalized frequencies agree with the 3D FDTD simulated results, as shown in the bottom of Fig. 6(c).

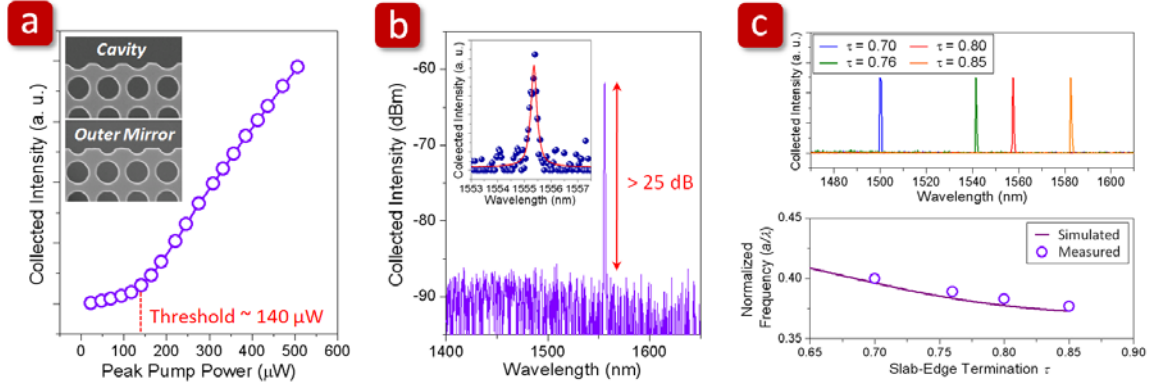


Fig. 6: (a) L - L curve and (b) lasing spectrum in dB scale of the DD_3 -mode from microcavity with $\tau = 0.80$ and $\Delta r/a = 0.09$. The zoom-in SEM pictures of the measured microcavity and the spectrum below threshold are shown as the insets of (a) and (b). (c) Lasing wavelengths of the DD_3 -mode under different τ from 0.70 to 0.85 (top), which agree with 3D FDTD simulation results (bottom) quite well.

(II) High Index Sensitivity of the Surface Mode via Gas Sensing

To address the potential of the $HPhC$ HSE microcavity serving as a high-sensitivity index sensor, we evaluate the R_n value by setting the environmental index from 1.00 (air) to 1.02 (with gases) in 3D FDTD simulations. The resulted R_n of 625 nm per refractive index unit variation (nm / RIU) is much higher than those of reported PhC defect cavities. To further increase the R_n value, the slab thickness is reduced from 220 nm to be 150 nm, which leads to more extended mode field outside the cavity and increases the sensitivity to the environmental index variation. In Table I, the simulated R_n value significantly increases from 625 to 720 nm / RIU with the reduced slab thickness. In experiments, the slab thickness is chosen as 180 nm due to the available epitaxial wafer.

To demonstrate optical index sensing functionality by $HPhC$ HSE microcavity, we set up a high vacuum chamber with a gas flow controlling gauge and a vacuum pump, as shown in Fig. 7(a). The device is mounted on a stage inside the chamber. The CO_2 gas pressure in chamber is controlled and tuned from 1.00×10^4 to 1.15×10^5 Pa. The measured surface mode wavelength shift is shown in Fig. 7(b), which indicates a linear red shift when the CO_2 gas pressure increases, that is, when the environmental index increases. This agrees quite well with the 3D FDTD simulation prediction also denoted in Fig. 7(b). The surface mode lasing spectra under CO_2 pressures of 1.00×10^4 and 1.15×10^5 Pa are shown in Fig. 7(c). The wavelength shift is 0.3 nm and the pressure variation leads to the refractive index change of 4.8×10^{-4} . Thus, we obtain a high R_n value of 625 nm / RIU in experiment, which agrees with the simulation result of 675 nm / RIU quite well. Considering the surface mode line width of 0.24 nm in Fig. 7(c), the experimental minimum detectable index variation Δn_{det} is about 4×10^{-4} .

Table I: 3D FDTD simulated R_n , mode volume, and Q factor of $HPhC$ HSE microcavities with different slab thicknesses.

Slab Thickness	R_n	Mode Volume	Q
220 nm	625 nm/RIU	$2.25 (\lambda/n)^3$	6.6×10^5
180 nm	675 nm/RIU	$2.14 (\lambda/n)^3$	3.2×10^5
150 nm	720 nm/RIU	$2.03 (\lambda/n)^3$	1.1×10^5

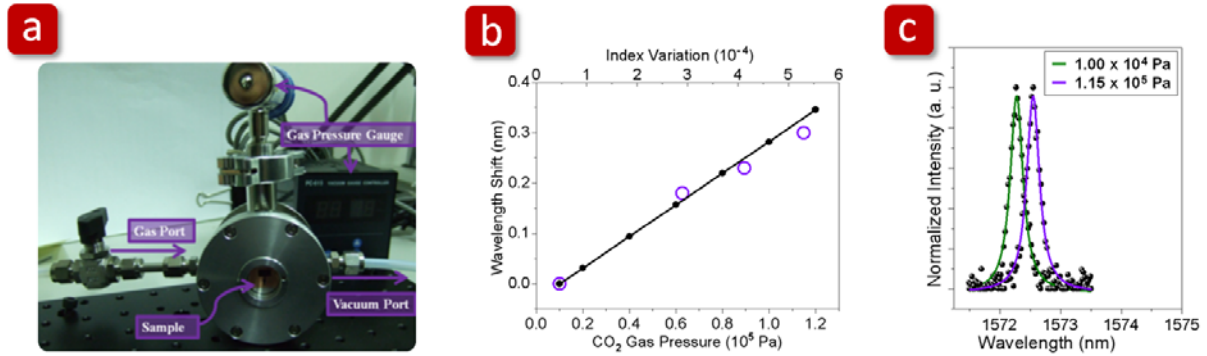


Fig. 7: (a) Picture of the high vacuum chamber with gas flow controlling gauge served as index sensor testing platform. (b) Measured (open circles) and simulated (solid dot line) wavelength shifts of surface mode under different CO_2 gas pressures and the corresponding index variations. (c) Surface mode lasing spectra under pressures of 1.00×10^4 and 1.15×10^5 Pa.

(III) Summary

In this section, we have proposed a brand new *PhC HSE* microcavity design via mode-gap effect, which can well confine the surface wave in the microcavity. The main achievements are listed below:

- A. **High simulated Q factor of 6.6×10^5** is obtained.
- B. Proximity correction design for *e*-beam lithography is developed to precisely control the device parameters.
- C. Single surface mode lasing with **low threshold of 140 μW** is observed.
- D. **High index sensing response R_n of 625 nm/RIU and small minimum detectable index variation Δn_{det} of 4×10^{-4}** are obtained via sensing CO_2 with different pressures in experiments, which show the strong possibilities for achieving highly sensitive optical sensors.

Related Publication:

1. Tsan-Wen Lu*, Shao-Pin Lu, Li-Hsun Chiu, and **Po-Tsung Lee**, "Square lattice photonic crystal surface mode lasers," *Opt. Express* **18**, pp. 26461-26468 (2010). (SCI IF: 3.935)
2. Tsan-Wen Lu*, Yi-Hua Hsiao, Wei-De Ho, and **Po-Tsung Lee**, "High Index Sensitivity of Surface Mode in Photonic Crystal Hetero-Slab-Edge Microcavity," *Opt. Lett.* **35**, pp. 1452-1454 (2010). (Cited: 2) (SCI IF: 3.546)
3. Tsan-Wen Lu*, Yi-Hua Hsiao, Wei-De Ho, and **Po-Tsung Lee**, "Photonic crystal hetero-slab-edge microcavity with high quality factor surface mode for index sensing," *Appl. Phys. Lett.* **94**, 141110 (2009). (Cited: 9) (SCI IF: 3.854)
4. Yi-Hua Hsiao, Tsan-Wen Lu*, Wei-De Ho, and **Po-Tsung Lee**, "High-Q Photonic Crystal Hetero-Slab-Edge Microcavity Laser for Index Sensing," CTuDD4, *IEEE/OSA CLEO/QELS'09*, Baltimore, Maryland, USA (2009).

II. *SPhC* POINT-SHIFTED D_0 NANOCAVITY FOR PROTEIN AND SINGLE NANO-PARTICLE DETECTION

In recent years, *PhC* nanocavities have shown the abilities of strongly controlling photons in a wavelength-scale resonator with very low optical losses, which lead to high Q factors and ultrasmall V . These *PhC* nanocavities with energy concentrated in one- or half-wavelength cubic volume show enhanced light-matter interactions and are very beneficial for thresholdless nanolasers and quantum-electro-dynamic phenomenon studies. Moreover, the ultrasmall nanocavity size would be very sensitive to the locally-induced perturbations, for example, nano-particles and bio-molecules, which are very advantageous for realizing highly sensitive optical bio-sensors. In this section, we propose an ultrasmall nanocavity design based on *SPhC*. The properties of defect modes are investigated and confirmed both in simulations and experiments. We also apply this nanocavity for sensing protein adsorption and spectral-free sensing single nano-particle.

(I) *Nanocavity Design and Modal Properties*

Scheme of our proposed *SPhC* point-shifted D_0 nanocavity design is shown in Fig. 8. The *SPhC* is defined by air holes on a suspended dielectric slab. The positions and radii r of four central air holes are shifted outward and shrunk to be r' , respectively, to form the nanocavity region. In 3D *FDTD* simulation, the lattice constant, slab thickness, r/a , and r'/a ratio are set to be 500 nm, 220 nm, 0.38, and varied from 0.285 to 0.36. From the simulation results, three defect modes exist in D_0 nanocavity with different r'/a ratios, including the whispering-gallery (*WG*), dipole, and monopole modes. The relationships between the simulated mode frequency and r'/a ratio of *SPhC* D_0 nanocavity are shown in Fig. 9(a). The simulated mode profiles in electrical fields are shown in Fig. 9(b). Owing to the potential of *WG* mode in electrically-driven nanolasers based on nanopost structure, we optimize the Q factor and mode volume of *WG* mode under different r'/a ratios. As we can see in Fig. 9(c), the maximum Q of 14,000 and minimum V of $5.5(\lambda/2n)^3$ are both obtained when $r'/a = 0.30$, which lead to a high Purcell factor of 1,500.

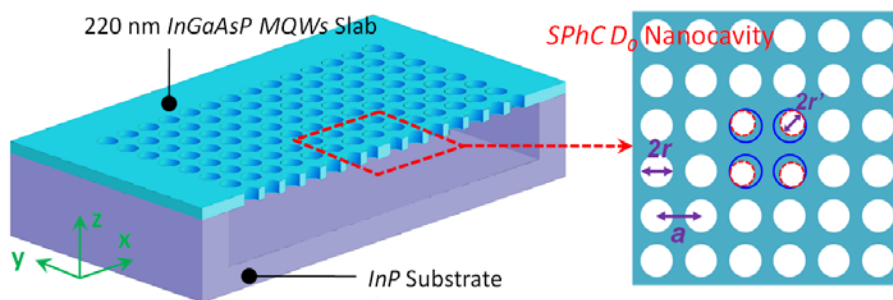


Fig. 8: Scheme of *SPhC* D_0 nanocavity on a suspended dielectric slab.

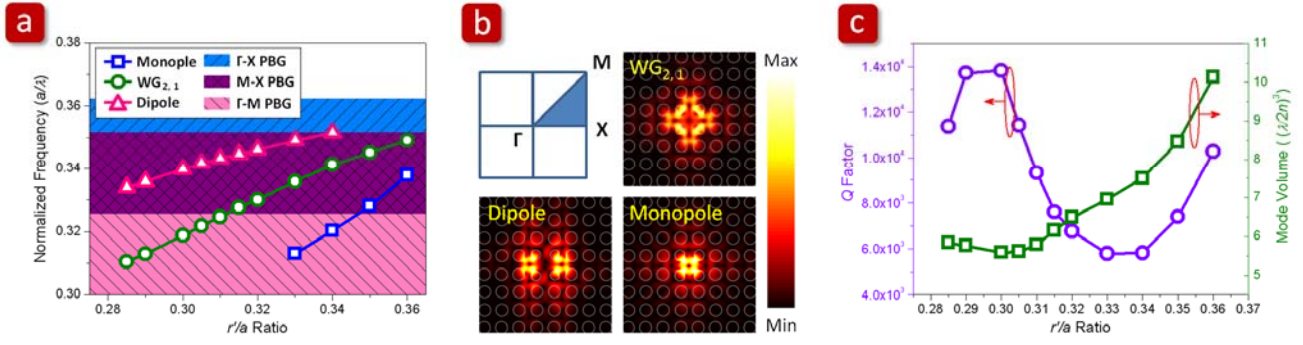


Fig. 9: (a) Plot of 3D FDTD simulated defect mode frequency versus r'/a ratio in $SPPhC D_0$ nanocavity under fixed r/a ratio of 0.38, including the WG, dipole, and monopole modes. (b) FDTD simulated mode profiles in electric fields of the three defect modes. (c) The simulated Q and V of WG mode in D_0 nanocavity under different r'/a ratios.

Top- and tilted-view SEM pictures of $SPPhC D_0$ nanocavity are shown in Fig. 10(a). With $a = 500$ nm, $r/a \sim 0.38$, and $r'/a = 0.30$, we obtain the WG single mode lasing at 1560 nm. The measured L - L curve and spectrum are shown in Figs. 10(b) and 10(c). The threshold is estimated to be 160 μ W (only 8 μ W is absorbed by the MQWs) from L - L curve. This low threshold directly indicates the potential in achieving thresholdless nanolasers, which is attributed to the small V and high Q factor of the WG mode in D_0 nanocavity. We also obtain the spectrum below threshold shown as the inset of Fig. 10(b). The spectral line width by Lorentzian fitting is 0.38 nm, which corresponds to a Q factor of 4,100. And the measured SMSR larger than 20 dB is shown as the inset of Fig. 10(c).

To observe and identify all the three modes in experiments, we measure $SPPhC D_0$ nanocavities with increased r'/a ratio from 0.285 to 0.34 and the measured single mode lasing wavelengths are shown in Fig. 11. Compared to the simulation results in Fig. 9(a), when r'/a ratio decreases, we can identify the lasing modes from top to bottom in Fig. 11 as the monopole, WG, and dipole modes. To further confirm this identification, the polarizations are measured and shown in Fig. 11. For the identified dipole mode, we obtain a high polarized degree (PD) of 0.93 and observe its wavelength splitting due to degeneracy breaking caused by the fabrication imperfection. In contrast, the WG and monopole modes both show low PD values of 0.08 and 0.19, respectively, because of the far-field cancellations of x - and y -electrical fields.

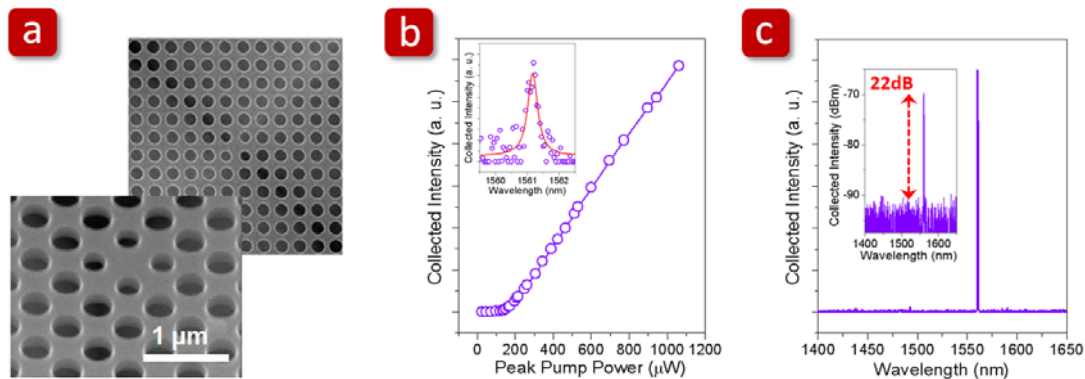


Fig. 10: (a) Top- and tilted-view SEM pictures of fabricated $SPPhC D_0$ nanocavity. (b) The measured L - L curve and (c) lasing spectrum of WG mode from $SPPhC D_0$ nanocavity. The measured WG mode spectrum below threshold and the lasing spectrum in logarithm scale are shown as the insets of (b) and (c).

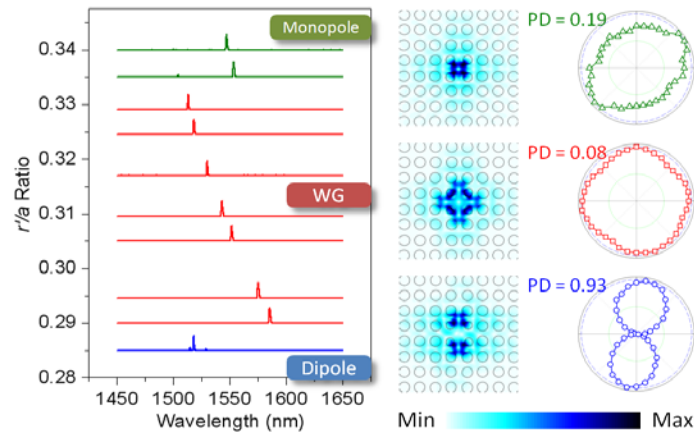


Fig. 11: The measured single mode lasing wavelengths under different r/a ratios of $SPnC D_0$ nanocavity. The simulated mode profiles in electrical fields and measured polarizations of the monopole, WG, and dipole modes are also shown.

(II) Post-Fabrication Process for Forming the Linking Layer at In-Organic / Organic Interface

Optically sensing protein (antigen/antibody), DNA, and virus via optical resonators hosts the advantages of label-free, real-time monitoring, and so on. It simplifies the traditional process with fluorescence label and is beneficial for fundamental studies in biological process, drug discovery, disease diagnosis and therapy. The ultrasmall nanocavity size would be very sensitive to the locally-induced perturbations arisen from the bio-molecules (protein, for example) and suitable for realizing highly sensitive optical bio-sensors. To apply our proposed device for protein sensing, first, we make a chemical treatment on $InGaAsP$ surface via 1-octadecanethiol (ODT, $HS(CH_2)_{17}CH_3$) to provide a linking layer at the organic / inorganic interface. Due to the straight alkane chains shown in Fig. 12(a), ODT can form a very ordered monolayer on InP and $GaAs$ surfaces by sulfur covalent attachments on In and As . Our developed process is illustrated below:

1. The $InGaAsP$ surface is cleaned by acetone and isopropanol (IPA) in sequence. It is then immersed in 48 % HF solution to remove the native oxide on surface and permit the following ODT monolayer formation.
2. After rinsed by deionized water and IPA, the surface is incubated in 0.15 mM ODT/ethanol solution over 24 hours. Then the surface is rinsed and dried by ethanol to remove unattached ODT residue.

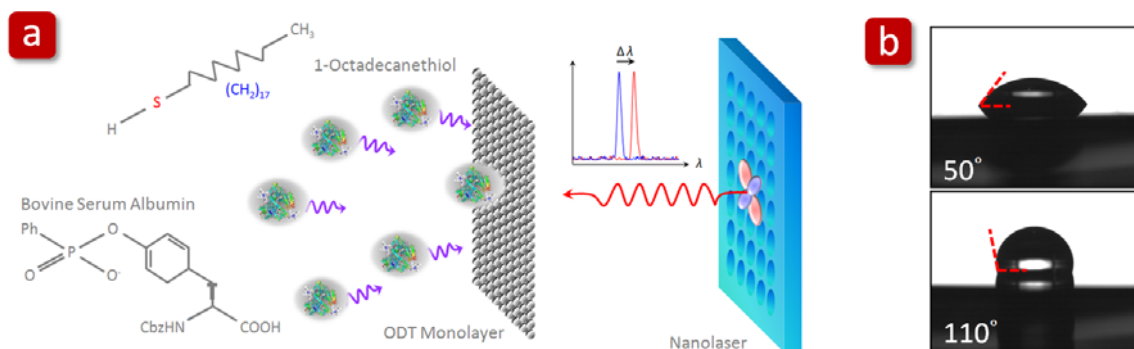


Fig. 12: (a) Scheme of protein adsorption and detection via ODT-treated $SPnC D_0$ nanocavity. (b) Measured contact angles of oxide-free $InGaAsP$ surfaces before (50°) and after (110°) ODT treatment.

To confirm the formation of *ODT* monolayer, we measure the contact angles of the oxide-free surfaces before and after *ODT* treatment, which are 50° and 110° , respectively, as shown in Fig. 12(b). This indicates the hydrophilic oxide-free surface becomes hydrophobic due to the *ODT* attachments. The *ODT* monolayer formation enables the following protein adsorption on CH_3 -terminated surface. The surface with *ODT* monolayer is then incubating in bovine serum albumin (*BSA*) / phosphate buffered saline with 1 mg/mL concentration at room temperature. Finally, the sample is rinsed by deionized water to remove weakly adsorbed *BSA* residue and dried. The surface becomes hydrophilic again, which indicates the protein adsorption. Then protein adsorption on the nanocavity surface will be detected by the wavelength shift of the defect mode, as illustrated in Fig. 12(a).

(III) Protein Adsorption Detection

The *SPhC* D_0 nanocavities with different r'/a ratios are treated by above process and then optically pumped by the fixed power of 0.6 mW at room temperature. Single mode lasing wavelengths of each defect mode are recorded before and after *BSA* adsorption, as shown in Fig. 13(a). The monopole, *WG*, and dipole modes show red shifts of 2.0, 1.8, and 1.2 nm in wavelength, which are arisen from the adsorbed protein on the D_0 nanocavity. To further confirm these observations, we apply *3D FDTD* method to simulate the wavelength shift of each mode. We assume the protein adsorbs on the entire surface of the D_0 nanocavity. The adsorbed protein is assumed to be with refractive index of 1.5 and its effective thickness is varied from 0 to 2 nm. The simulated results are shown in Fig. 13(b). By matching the measured results with the simulated ones, we can obtain an effective protein thickness of 1.55 nm. Considering the defect mode field distribution of only four-lattice-constant distance from the D_0 nanocavity, the interrogated analyte amount can be less than 2.2 fg. Furthermore, when we consider the spectral line width of the lasing mode, for example, 0.6 nm for *WG* mode, the minimum measurable protein amount is less than 0.8 fg, which indicates the high sensitivity of our device.

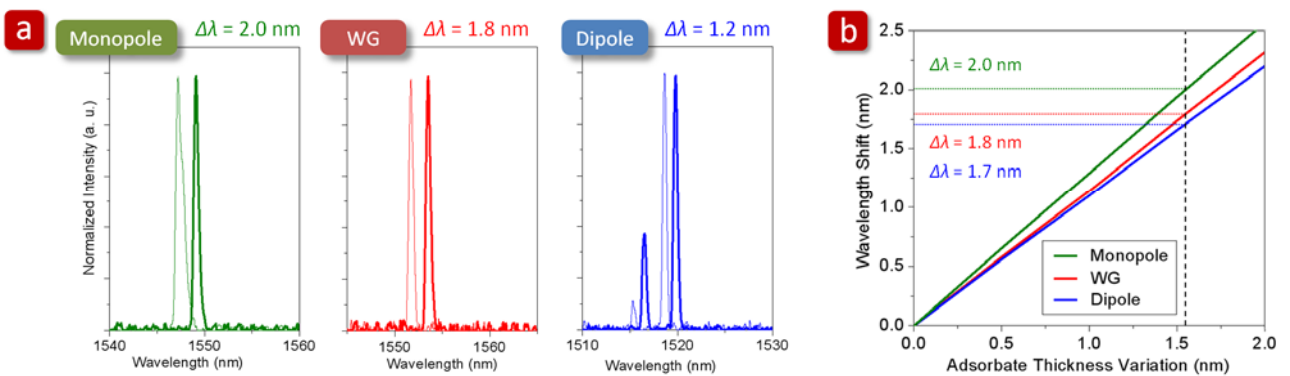


Fig. 13: (a) The measured single mode lasing spectra of the monopole, *WG*, and dipole modes before (solid-line) and after (bold solid-line) the protein (*BSA*) adsorption. (b) *3D FDTD* simulated wavelength shifts of the monopole, *WG*, and dipole modes (from top to bottom) contributed from the adsorbed protein on the entire D_0 nanocavity surface.

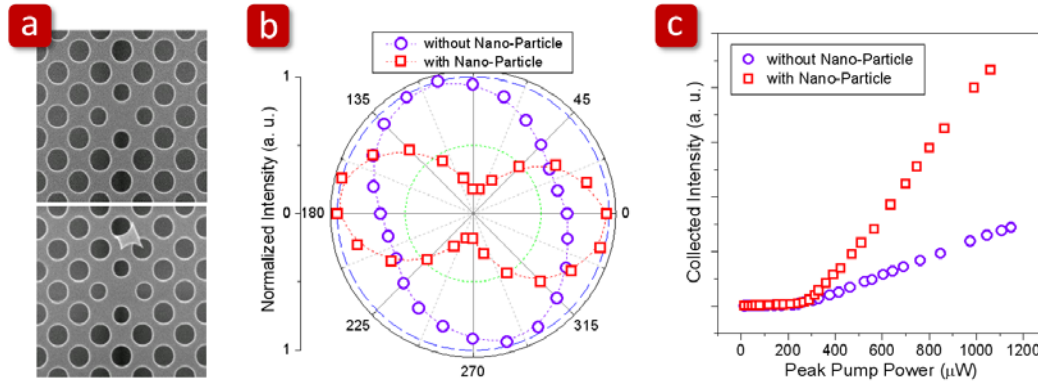


Fig. 14: (a) Top-view SEM pictures of $SPnC D_0$ nanocavities (top) without and (bottom) with a 350 nm NP nearby. The measured (b) polarizations and (c) $L-L$ curves of WG mode in $SPnC D_0$ nanocavities with and without a NP nearby.

(IV) Spectrum-Free Detection of Nano-Particle

As we can see in Fig. 11, the WG mode shows a very low PD value due to the electric field cancellation in the far field. In reality, this low-polarized property can be broken by deliberate designs or fabrication non-uniformities and the WG mode will become polarized. Thus, a very local perturbation, for example, a dielectric nano-particle (NP) nearby the nanocavity, can be detected via the polarization variation.

We compare the WG mode lasing actions from $SPnC D_0$ nanocavities with and without a 350 nm-diameter dielectric NP nearby, as shown in Fig. 14(a). From the measured polarizations in Fig. 14(b), obviously, the PD increases to be 0.69 when there is a NP nearby the nanocavity. This strong influence is attributed to the comparable sizes between D_0 nanocavity and the NP . The measured $L-L$ curves of these two cases are shown in Fig. 14(c). The slope efficiency increases significantly when the NP is presented. This is because when the NP breaks the modal symmetry of WG mode, it also breaks the WG modal cancellation in the far field. Thus, there will be more radiation components collected by the objective lens and lead to the increased slope efficiency.

This observed unique behavior of WG mode based on polarization variation could be a spectral-free and effective approach to detect single NP . This means the requirement of very high Q factors in PhC nanocavities by very delicate modulations is not essential for detection down to single molecule binding or attaching via this approach.

(V) Summary

In this section, we propose a D_0 nanocavity formed by shifting and shrinking the four central air holes of $SPnC$ for sensing protein adsorption and spectral-free detecting single NP . The main achievements are listed below:

- A. The defect modes in the D_0 nanocavity are investigated and optimized for nanolasers both in simulations and experiments. Single WG mode lasing with high measured **Q factor of 4,100** and **low threshold of 160 μW** is obtained.
- B. We develop a chemical treatment process on $InGaAsP$ surface to form the ODT linking monolayer, which enables the following protein (BSA) adsorption.

- C. Via the experimentally observed wavelength shifts of lasing modes due to the BSA adsorption, very **small minimum measureable protein amount less than 0.8 fg** can be achieved via the WG mode in this nanocavity.
- D. We observe WG modal symmetry breaking due to a 350 nm dielectric NP nearby the D_0 nanocavity in experiments. This polarization variation could be used as a **spectral-free approach** to sense single molecule binding and attaching in bio-chemical or drug discovery researches, where very high Q factor is not required.

It is worthy to note the result of C published in [*Appl. Phys. Lett.* **96**, 213702 (2010)] is selected for *Virtual Journal of Nanoscale Science & Technology*, **Vol. 21**, issue 23, Jun. 7, 2010, *Virtual Journal of Biological Physics Research*, **Vol. 19**, issue 11, Jun. 1, 2010, and *Physics Communications in Taiwan*, Jul. 15, 2010. In addition, the result of D published in [*Opt. Express* **18**, pp. 2566-2572 (2010)] is selected for *Virtual Journal of Biomedical Optics*, **Vol. 5**, issue 4, Feb. 26, 2010.

Related Publication:

1. Tsan-Wen Lu*, Pin-Tso Lin, Kuan-Un Sio, and **Po-Tsung Lee**, "Optical sensing of square lattice photonic crystal point-shifted nanocavity for protein adsorption detection," *Appl. Phys. Lett.* **96**, 213702 (2010). (Cited: 4) (SCI IF: 3.854)
(Selected for *Virtual Journal of Nanoscale Science & Technology*, **Vol. 21**, issue 23, Jun. 7, 2010)
(Selected for *Virtual Journal of Biological Physics Research*, **Vol. 19**, issue 11, Jun. 1, 2010)
(Selected for *Physics Communications in Taiwan*, Jul. 15, 2010)
2. Tsan-Wen Lu*, Pin-Tso Lin, Kuan-Un Sio, and **Po-Tsung Lee**, "Square lattice photonic crystal point-shifted nanocavity with lowest-order whispering-gallery mode," *Opt. Express* **18**, pp. 2566-2572 (2010). (Cited: 1) (SCI IF: 3.935)
(Selected for *Virtual Journal of Biomedical Optics*, **Vol. 5**, issue 4, Feb. 26, 2010)
3. Tsan-Wen Lu*, Pin-Tso Lin, Kuan-Un Sio, and **Po-Tsung Lee**, "Square Lattice Photonic Crystal Point-Shifted D_0 Nanocavity with Lowest-Order Whispering-Gallery Mode," CWK5, IEEE/OSA CLEO/QELS'10, San Jose, California, USA (2010).

III. MULTI-FUNCTIONAL TWO-DIMENSIONAL HONEYCOMB PhC SLAB

Unlike the above PhC cavity lasers that confine photons in a defect region created inside the PhC by the TIR and PBG effects, the PhC band-edge (BE) laser utilizes the flat photonic band with local group velocity $v_g \sim 0$ near high symmetric points to enhance light-gain interactions and achieves lasing operations. Generally, the BE modes can be classified into the slab-confined and radiative modes, whose frequencies lie below and above the light line, respectively. For the radiative mode, especially near Γ point, there are several unique features beneficial for the optical lasers and sensors:

- A. Lasing of radiative mode occurs near Γ point with almost zero in-plane wave vector summation and thus has directional surface laser emission.
- B. The high power single mode lasing emission indicates high SMSR for lasers and high signal/noise (S/N) ratio for optical sensors.
- C. Because the BE mode lasing occurs in PhC structure with large area and without delicate defect design, this type of device is suitable for high throughput fabrication processes with large fabrication tolerance, such as holographic lithography and nano-imprint technologies.

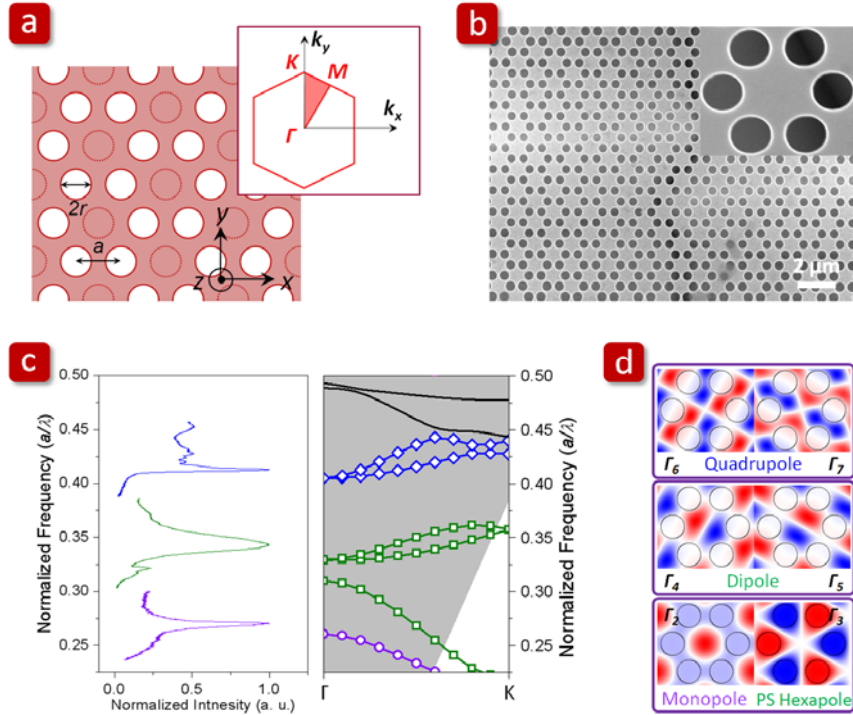


Fig. 15: (a) Scheme and (b) SEM pictures of a 2D honeycomb PhC slab. The first and irreducible Brillouin zones are also shown as the inset of (a). (c) The measured spectra from the 2D honeycomb PhC slabs with different lattice constants and 3D PWE simulated TE-like Γ -K band diagram. (d) The simulated mode profiles in magnetic fields for modes near Γ_2 to Γ_7 .

(I) BE Modes near Γ Point in 2D Honeycomb PhC Slab

In addition to the BE modes in SPhC and HPhC, the honeycomb PhC with flat BE bands near Γ point also attracts lots of attention for BE mode lasers because of several unique features:

- A. Lower air-filling factor** than those of the SPhC and HPhC owing to less air holes
- B. Less non-radiative recombination**
- C. Larger gain volume**
- D. Better heat dissipation**

All of these are advantageous for active light emitting devices. Here we demonstrate and identify the monopole, quadrupole, and dipole modes near Γ point in 2D honeycomb PhC slabs, while the applications for microlasers, highly sensitive optical sensors, and broad band-width light emission enhancement from these modes are also demonstrated.

The 2D honeycomb PhC lattice is obtained from the HPhC lattice with periodic missing air holes on a suspended InGaAsP slab shown in Fig. 15(a). The air hole radius (r), lattice constant (a), first and irreducible Brillouin zones of the honeycomb PhC are defined in Fig. 15(a). Top-view SEM pictures of a 2D honeycomb PhC slab and its lattice cell are shown in Fig. 15(b). In measurements, we observe different resonance peaks from the fabricated slabs with different lattice constants at low excitation power, as shown in Fig. 15(c). To address these peaks, the transverse-electric-like (TE-like) band diagram is obtained by 3D plane-wave expansion (PWE) simulation, as shown in Fig.

15(c). Comparing the measured and simulated results, we can identify these peaks from low to high frequencies as Γ_2 (monopole mode), Γ_3 (phase-shifted (PS) hexapole mode), $\Gamma_{4,5}$ (dipole modes), and $\Gamma_{6,7}$ (quadrupole modes). The corresponding simulated mode profiles in magnetic fields are shown in Fig. 15(d). Among these modes, the monopole and PS hexapole modes are non-degenerate modes and the others are degenerate modes.

(II) Applications for Lasers, Optical Sensors, and High Brightness Light Emitters

According to the initial mode identifications in Figs. 15(c) and (d), the 2D honeycomb PhC slabs with different parameters are fabricated and characterized for the monopole ($a = 420 - 450$ nm, $r/a = 0.38 - 0.44$) and quadrupole ($a = 620 - 650$ nm, $r/a = 0.38 - 0.44$) modes. For microlaser applications, the measured L - L curve and lasing spectrum in dB scale of the monopole mode are shown in Figs. 16(a) and (b), which show lasing threshold of 1.6 mW and high SMSR of 35 dB, respectively. To further confirm the lasing mode as the monopole mode, the normalized monopole mode frequencies with different r/a ratios and fixed lattice constant obtained by 3D PWE method are compared to the measured results, as shown in Fig. 16(a). In addition, the quadrupole mode also shows high SMSR larger than 30 dB, but the threshold of 5.4 mW is much higher than that of the monopole mode.

High SMSRs of the monopole and quadrupole modes not only meet the requirement for microlasers in optical communication systems but also indicate high S/N ratios when serving as optical sensors. To investigate the performances of these two lasing modes for optical sensing, we immerse the samples in different transparent index matching liquids and obtain their lasing spectra. For the quadrupole mode, as shown in Fig. 16(c), the wavelength shift reaches 30 nm under 0.08 refractive index variation from 1.30 to 1.38, which leads to a relatively high R_n value of 375 nm/RIU via linear fitting shown as the inset of Fig. 16(c). This high R_n value agrees with the simulated value of 383 nm/RIU. By considering the measured narrowest lasing spectral line width of 0.13 nm, the minimum detectable index variation Δn_{det} is as low as 3.5×10^{-4} , which is comparable with those from carefully-designed PhC micro- and nano-cavities and much higher than those demonstrated by PhC BE lasers. However, for the monopole mode, the measured R_n value is only 70 nm/RIU, which is much lower than that of the quadrupole mode.

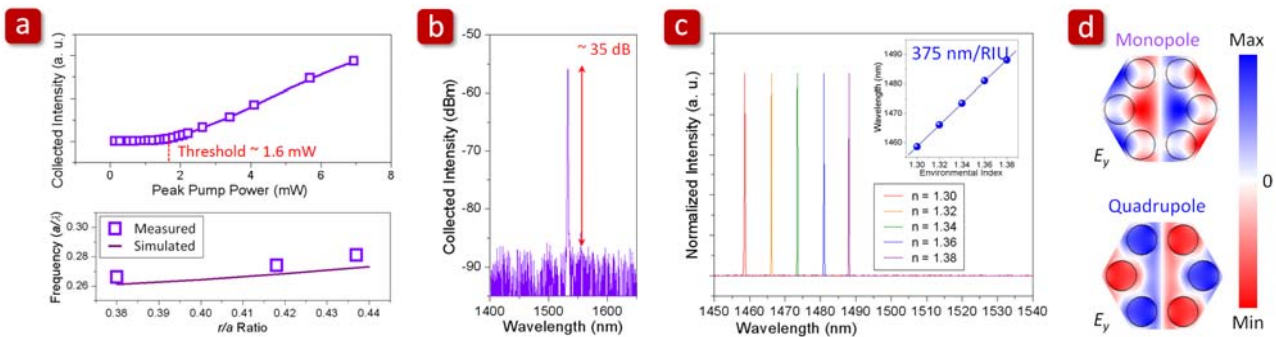


Fig. 16: The measured (a) L - L curve and (b) lasing spectrum in dB scale of lasing action from the monopole mode. The 3D PWE simulated monopole mode frequencies with different r/a ratios and fixed lattice constant is also shown in (a). (c) The measured lasing spectra of the quadrupole mode with total index variation of 0.08. The wavelength shift fitting curve is shown as the inset with R_n value of 375 nm/RIU. (d) 3D PWE simulated E_y fields of the monopole and quadrupole modes in a honeycomb PhC cell in x - y plane.

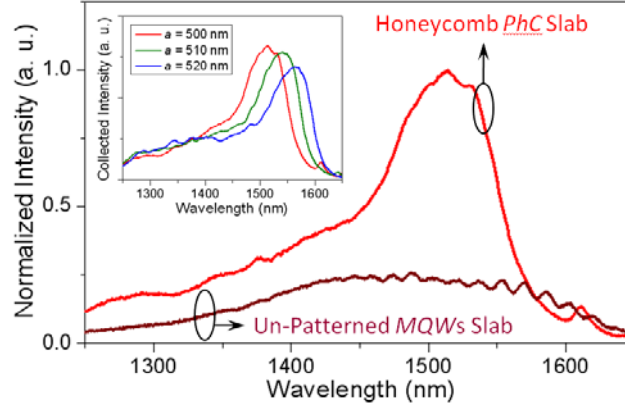


Fig. 17: The measured PL spectra from the 2D honeycomb PhC and un-patterned MQWs slabs. Over five-fold PL enhancement near wavelength of 1510 nm attributed to the dipole mode near Γ point is observed. The enhanced PL spectra under different lattice constants from 500 to 520 nm are also shown as the inset.

From above measured results, we can conclude that the monopole and quadrupole modes in the 2D honeycomb PhC slabs are suitable for microlaser and sensor applications, respectively. The differences between these two modes in different applications can be understood by the 3D PWE simulated E_y fields in x-y plane shown in Fig. 16(d). The E_y field of the monopole mode tends to distribute more in the dielectric region than that of the quadrupole mode, which shows that the monopole mode has less radiation field extending into the air. Thus, the monopole mode has good mode field overlap with the dielectric gain region and is less sensitive to the environmental index variation, which lead to lower lasing threshold and smaller R_n value than those of the quadrupole mode in experiments.

We also characterize the 2D honeycomb PhC slab with $a = 500$ nm and $r/a = 0.36$ for the dipole mode. Over five-fold PL enhancement compared to the un-patterned MQWs slab is shown in Fig. 17, which is confirmed as the dipole mode by 3D PWE simulations. This enhancement is attributed to the lossy feature of the dipole mode, which leads to much easier coupling of the mode energy into the air than the other modes. To further verify this PL enhancement from the dipole mode, the enhanced PL spectra of devices with different lattice constants from 500 to 520 nm are shown as the inset of Fig. 17. The red-shift of PL peak with increased lattice constant is observed and agrees with both 3D PWE and FDTD simulation results. Moreover, the PL enhancement from the dipole mode is with broad band-width of 100 nm, which is broader than the monopole and quadrupole modes with narrow band-widths shown in Fig. 15(c). Thus, based on the dipole mode, we believe the honeycomb PhC structure with low air-filling factor is suitable to be applied to enhance light extraction for high brightness LEDs.

(III) Summary

In this section, we have studied the BE modes near Γ point of the 2D honeycomb PhC slabs. This kind of PhC structure has advantages of low air-filling factor, less surface recombination, large gain volume, and good heat dissipation for optoelectronic devices. The main achievements in different applications via the BE modes near Γ point of the 2D honeycomb PhC slabs are listed below.

- A. Single mode lasing with **high SMSR of 35 dB** is obtained from the monopole mode.

- B. High index sensing response R_n of 375 nm/ RIU and ultrasmall minimum detectable index variation Δn_{det} of 3.5×10^{-4} are obtained via the quadrupole mode.
- C. Over five-fold PL enhancement with > 100 nm broad band-width is obtained from the dipole mode at room temperature, which is beneficial for designing high brightness $LEDs$.

Related Publication:

1. **Po-Tsung Lee**, Tsan-Wen Lu*, and Kuan-Un Sio, "Multi-Functional Light Emitter Based on Band-Edge Modes near F -Point in Honeycomb Photonic Crystal," *J. Lightwave Technol.* **29**, pp. 1797-1801 (2011). (SCI IF: 2.563)

IV. DOUBLE-LAYERED PhC MICROCAVITIES FOR OPTICALLY SENSING STRESS

So far, we have demonstrated the optical index and protein sensors based on different PhC lasers. Optical stress sensor is another important component in mechanical and semiconductor applications, especially in optical micro-electromechanical systems. Although some interesting optical stress sensor designs based on PhC slabs and waveguides have been reported, the designs based on high Q micro- or nano-cavities are still hard to find in literatures and the sensitivity of present designs can be further improved. In this section, we will briefly illustrate the design principles of a highly sensitive optical stress sensor. According to the requirements, we introduce a structural design composed of doubled-layered (DL) PhC microcavities. The basic modal properties, structural variations, and corresponding optical spectrum response of DL PhC microcavities are investigated by $3D$ $FDTD$ and finite-element method (FEM) simulations.

(I) Design Principles of DL PhC Microcavities

First, for a designed stress sensor structure, we have to find the relationship between the applied stress and the corresponding structural variation. And then the relationship between the structural variation and the corresponding wavelength shift should be figured out. According to these two relationships, we can estimate the applied stress by the measured optical spectrum shift and decide how small the detectable stress variation per wavelength unit (in newton unit per optical wavelength shift in nanometer, N/nm) is. Furthermore, we can exactly define the minimum detectable stress variation (δF , in newton unit) by considering the minimum spectral line width of the measured light wave. Thus, we can define a simple equation to illustrate this relationship:

$$\delta F = \frac{\Delta F}{\Delta d} \times \frac{\Delta d}{\Delta \lambda} \times \frac{\lambda}{Q} = \frac{\lambda}{SWQ} \quad (1)$$

where $\Delta F / \Delta d$ and $\Delta d / \Delta \lambda$ represent the applied stress needed to cause specific structural variation and the structural variation needed to cause specific wavelength shift, respectively. From equation (1), we find the highly sensitive optical stress sensor can be achieved by small $\Delta F / \Delta d$ and $\Delta d / \Delta \lambda$. In addition, high Q factor of the microcavity is also necessary to achieve small δF . For simplicity, we define factors of $S = \Delta d / \Delta F$ and $W = \Delta \lambda / \Delta d$ to represent the structural variation rate due to the applied stress and wavelength shift rate due to the structural variation, respectively. And the δF can be expressed as λ / SWQ in equation (1).

(II) Modal Properties for Stress Sensing

Based on our previously-proposed *PhC CD₂* microcavity design with high *Q* *WG* mode shown in Fig. 18, we design a novel *DL PhC* microcavity structure composed by two identical *PhC CD₂* microcavity slabs, as shown in Fig. 18. By using *3D FDTD* simulation, we obtain bonding and anti-bonding modes in *DL PhC* microcavities and their mode profiles in electric fields are shown in Fig. 19(a). The relationships between wavelengths of bonding and anti-bonding modes and air-gap distance *d* are shown in Fig. 19(b). We investigate the *Q* variation of bonding mode under different *d*, which is shown in Fig. 19(c). We obtain a high enhanced *Q* of 110,000 when *d* = 550 nm. We also show *W* factors under different *d* in Fig. 19(c). Although the highest *Q* is available when *d* = 550 nm, the *W* factor at this *d* value is smaller than the cases with smaller *d*. Since the δF in equation (1) depends both on the *Q* and *W* factors, we can conclude there will be a trade-off between the *Q* and *W* factors for small δF .

In addition, to obtain high *S* factor in equation (1), we present a geometry named bridge-with-wings (*BwWs*), as shown in Fig. 20(a), where the *PhC* microcavity and the point stress are defined and applied on the wing and bridge regions, respectively. The separation of stress applying region (bridge) and sensing region (wings, *PhC* microcavities) guarantees the uniform displacement between the double layers when a stress is applied. The *FEM* simulated air-gap displacement Δd and torsion distribution when *F* = 50 nN are shown in Figs. 20(b) and (c). In Fig. 20(b), the maximum Δd is 3.3 nm in the *PhC* region, which corresponds to non-uniformity of 6.6%. Furthermore, in Fig. 20(c), the torsion mainly distributes in the bridge region and is close to zero in

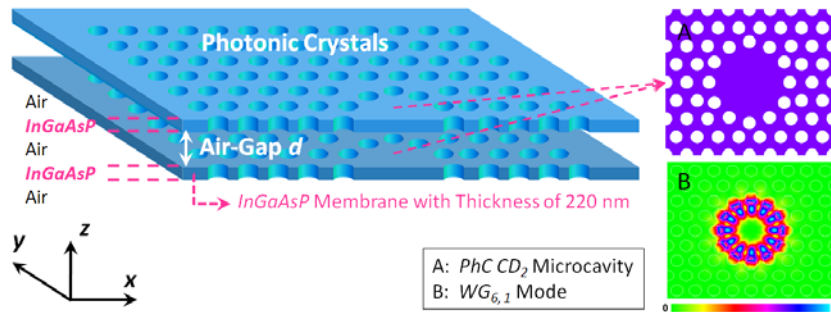


Fig. 18: Scheme of *DL PhC CD₂* microcavity slab. The microcavity design and the simulated *WG* mode profile in electric field are shown as the right insets A and B.

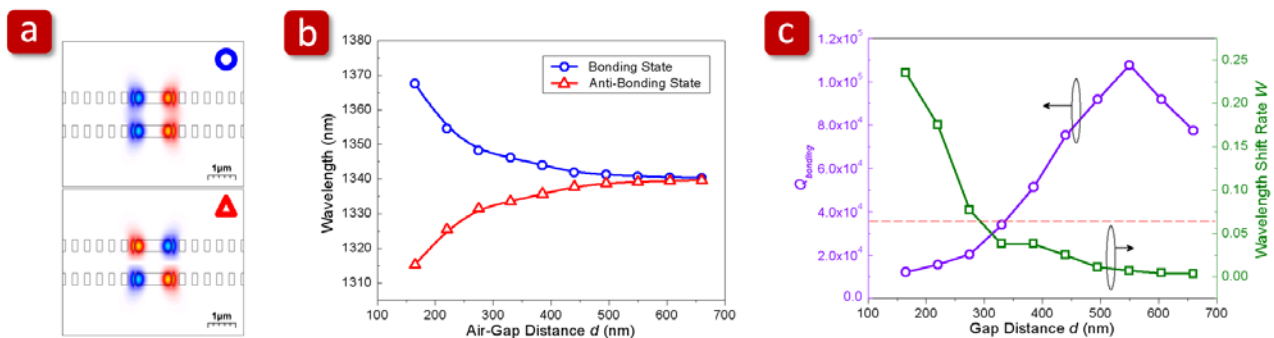


Fig. 19: (a) The simulated mode profiles in electric fields in *x-z* plane of bonding (top) and anti-bonding (bottom) modes. (b) The simulated wavelengths of bonding and anti-bonding modes versus the air-gap distance *d*. (c) The simulated *Q* and *W* factors of bonding mode for *d* varied from 165 to 660 nm.

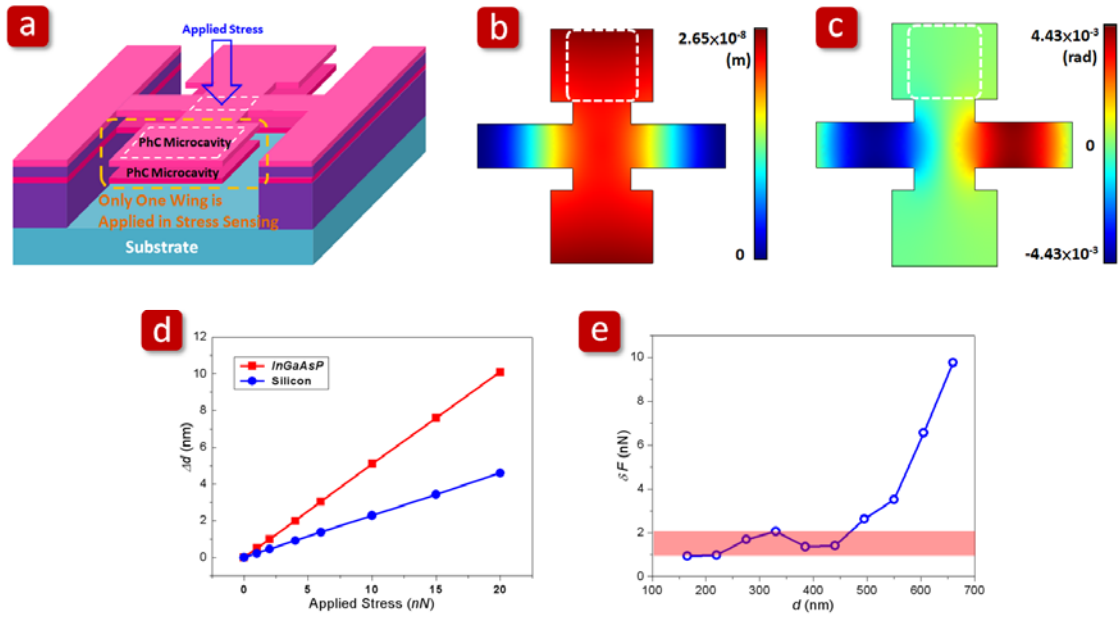


Fig. 20: (a) Scheme of DL PhC microcavities in BwWs geometry. The simulated (b) air-gap displacement Δd and (c) torsion distribution of the InGaAsP BwWs geometry when $F = 50$ nN. (d) The simulated relationships between the applied stress and Δd from BwWs geometry based on Si and InGaAsP materials. (e) The calculated minimum detectable stress variation δF for the BwWs geometry under different air-gap distances d .

the wing region. Via FEM simulation, we obtain the relationship between the applied stress F and Δd , as shown in Fig. 20(d). The calculated structural variation rates S of the BwWs geometry are 0.507 and 0.229 nm/nN for InGaAsP and silicon (Si) materials, respectively. We should note that the S factors using Si material are twice smaller than those using InGaAsP, which means twice structural response for applied stress by using InGaAsP instead of Si under the same geometric design.

According to equation (1) and combining FEM and FDTD simulation results, we can obtain δF of BwWs geometry when $d = 165 - 660$ nm, as shown in Fig. 20(e). The smallest δF is only 0.95 nN when $d = 165$ nm. We also find that the δF can be maintained nearly constant at a low value around 1 to 2 nN under a large range of initial d (165 - 440 nm) as indicated by the shadow region in Fig. 20(e), which provides a large design and fabrication tolerances in keeping high sensitivity. Thus, we believe this DL PhC microcavity design is promising in demonstrating ultrahigh sensitivity optical stress sensors.

(III) Summary

In this section, we present the design principles to obtain a highly sensitive optical stress sensor via novel DL PhC CD_2 microcavities with high Q $WG_{6,1}$ mode. The main achievements are listed below:

- A. The optical bonding and anti-bonding states in this microcavity structure analog to the energy states in chemical molecule are investigated and addressed theoretically.
- B. We illustrate the principles of designing highly sensitive optical stress sensors via the presented DL PhC CD_2 microcavities based on the bonding mode. Large optical response W

of 0.235 nm per 1 nm air-gap decrement when $d = 165$ nm, high $Q_{bonding} > 10^4$ under different d for fine spectral resolution, and large structural response S value of 0.507 nm / nN from *InGaAsP* BwWs geometry are obtained and all beneficial for realizing highly sensitive optical stress sensors.

- C. The minimum detectable stress variation δF is estimated to be as small as **0.95 nN** when $d = 165$ nm. In addition, the δF can be maintained **nearly constant at a low value around 1 to 2 nN** under a large range of initial d from 165 to 440 nm, which provides large design and fabrication tolerances.

This *DL PhC* microcavity design is very promising and feasible for optical stress sensors. Further improved sensitivity can be obtained by employing *PhC* micro- and nano-cavities with ultrahigh Q factors if required.

Related Publication:

1. Tsan-Wen Lu* and **Po-Tsung Lee**, "Ultra-high sensitivity optical stress sensor based on double-layered photonic crystal microcavity," *Opt. Express* **17**, pp. 1518-1526 (2009). (Cited: 10) (SCI IF: 3.935)

Conclusions

In this project, we have designed various *2D PhC* cavities formed by different mechanisms, including point-shifted nanocavity, surface modes in hetero-slab-edge, band-edge modes in honeycomb *PhC* slabs, and double-layered microcavities. Via realizing them in the form of semiconductor lasers, the observed low thresholds, high *Q* factors, and compact device sizes show their potential in serving as promising light source in *PICs*. Most importantly, we have demonstrated the functionalities of optical sensing with very high sensitivity via our presented *PhC* devices. The observations in experiments strongly indicate these *2D PhC* lasers are capable of sensing very slight index variations (for gas and liquid analytes), single virus-sized dielectric nano-particle, and protein adsorption. Owing to the compact device sizes, we believe these devices can be served as the highly sensitive, label-free, and ultra-compact optical sensors on an integrated bio-chip for fundamental studies of biological process, drug discovery, disease diagnosis and therapy.

Publications during the Project Period (2009-2011)

In the past two years, we have published 18 papers on famous international journals and letters in Applied Physics and Optics, including *Applied Physics Letters* (SCI IF: 3.854), *Optics Express* (SCI IF: 3.935), *Optics Letters* (SCI IF: 3.546), and so on. Some of them are regarded as highly impressive papers and selected for *Virtual Journal of Nanoscale Science & Technology*, *Virtual Journal of Biological Physics Research*, *Virtual Journal of Biomedical Optics*, *Physics Communications in Taiwan*, and *Top 20 Most Downloaded Papers (#6) of Aug. 2011 in Applied Physics Letters*. Excluding my own students, I am the only author of the 14 publications. Most of the published papers have been cited by other groups. The statistics and details of SCI IF, ranking factor, and citation number of our publications are shown in Table II. The publication list (2009-2011) is also provided below.

Table II: The SCI IF, ranking factor, and citation number of our publications in recent two years (2009 - 2011).

SCI IF Distribution of 18 Publications in 2009 – 2011					
SCI IF > 3.0	10	2.0 < SCI IF < 3.0	7	SCI IF < 2.0	1
SCI Ranking Factor of 18 Publications in 2009 – 2011					
< 5 %	3	> 5%, < 20 %	14	> 20 %	1
Citation Number of 18 Publications in 2009 – 2011					
Total	56	by Others	49	Self-Cited	7

Publication List (2009-2011)

(I) International Letter & Journal Articles (Based on 2010 5-Year SCI IF)

1. Tsan-Wen Lu, Li-Hsun Chiu, Pin-Tso Lin, and **Po-Tsung Lee***, "One-dimensional photonic crystal nanobeam lasers on a flexible substrate," *Appl. Phys. Lett.* **99**, 071101 (2011). (SCI IF: 3.854)
(Top 20 Most Downloaded Papers (#6) of Aug. 2011 in *Appl. Phys. Lett.*)
2. **Po-Tsung Lee**, Tsan-Wen Lu*, and Kuan-Un Sio, "Multi-Functional Light Emitter Based on Band-Edge Modes near Γ -Point in Honeycomb Photonic Crystal," *J. Lightwave Technol.* **29**, pp. 1797-1801 (2011). (SCI IF: 2.563)
3. Chia-Yang Tsai*, Shao-Ping Lu, Jyun-Wei Lin, and **Po-Tsung Lee**, "High sensitivity plasmonic index sensor using slab-like gold nanoring arrays," *Appl. Phys. Lett.* **98**, 153108 (2011). (Cited: 1) (SCI IF: 3.854)
(Selected for *Virtual Journal of Nanoscale Science & Technology*, Vol. 23, issue 16, Apr. 25, 2011)
(Selected for *Physics Communications in Taiwan*, Aug. 11, 2011)
4. Pin-Tso Lin* and **Po-Tsung Lee**, "All-optical controllable trapping and transport of subwavelength particles on a tapered photonic crystal waveguide," *Opt. Lett.* **36**, pp. 424-426 (2011). (SCI IF: 3.546)
(Selected for *Virtual Journal of Biomedical Optics*, Vol. 6, issue 3, Mar. 18, 2011)
5. Tsan-Wen Lu*, Shao-Pin Lu, Li-Hsun Chiu, and **Po-Tsung Lee**, "Square lattice photonic crystal surface mode lasers," *Opt. Express* **18**, pp. 26461-26468 (2010). (SCI IF: 3.935)
6. Tzu-Yueh Chang*, Chun-Lung Chang, Hsin-Yu Lee, and **Po-Tsung Lee**, "A metal-insulator-semiconductor solar cell with high open-circuit voltage using a stacking structure," *IEEE Electron. Device Lett.* **31**, pp. 1419-1421 (2010). (SCI IF: 2.607)

7. Tsan-Wen Lu*, Pin-Tso Lin, Kuan-Un Sio, and **Po-Tsung Lee**, "Optical sensing of square lattice photonic crystal point-shifted nanocavity for protein adsorption detection," *Appl. Phys. Lett.* **96**, 213702 (2010). (Cited: 4) (SCI IF: 3.854)
(Selected for *Virtual Journal of Nanoscale Science & Technology*, Vol. 21, issue 23, Jun. 7, 2010)
(Selected for *Virtual Journal of Biological Physics Research*, Vol. 19, issue 11, Jun. 1, 2010)
(Selected for *Physics Communications in Taiwan*, Jul. 15, 2010)
8. Tsan-Wen Lu*, Yi-Hua Hsiao, Wei-De Ho, and **Po-Tsung Lee**, "High Index Sensitivity of Surface Mode in Photonic Crystal Hetero-Slab-Edge Microcavity," *Opt. Lett.* **35**, pp. 1452-1454 (2010). (Cited: 2) (SCI IF: 3.546)
9. Tzu-Yueh Chang*, You-Wei Cheng, and **Po-Tsung Lee**, "Electrical characteristics of an organic bistable device using an Al/Alq₃/nanostructured MoO₃/Alq₃/p⁺-Si structure," *Appl. Phys. Lett.* **96**, 043309 (2010). (Cited: 6) (SCI IF: 3.854)
10. Tsan-Wen Lu*, Pin-Tso Lin, Kuan-Un Sio, and **Po-Tsung Lee**, "Square lattice photonic crystal point-shifted nanocavity with lowest-order whispering-gallery mode," *Opt. Express* **18**, pp. 2566-2572 (2010). (Cited: 1) (SCI IF: 3.935)
(Selected for *Virtual Journal of Biomedical Optics*, Vol. 5, issue 4, Feb. 26, 2010)
11. Wei-De Ho, Tsan-Wen Lu*, Yi-Hua Hsiao, and **Po-Tsung Lee**, "Thermal Properties of 12-Fold Quasi-Photonic Crystal Microcavity Laser with Size-Controlled Nano-Post for Electrical Driving," *J. Lightwave Technol.* **27**, pp. 5302-5307 (2009). (Cited: 4) (SCI IF: 2.563)
12. Chia-Ho Chen, Tsan-Wen Lu*, and **Po-Tsung Lee**, "Microcavity Laser Emissions Based on Double Hetero-Structure by Locally Modulated Photonic Crystal Waveguide," *J. Lightwave Technol.* **27**, pp. 4393-4400 (2009). (Cited: 1) (SCI IF: 2.563)
13. Ming-Feng Chang, **Po-Tsung Lee**, and Albert Chin, "Low Threshold Voltage MoN/HfAlO/SiON p-MOSFETs with 0.85-nm EOT," *IEEE Electron. Device Lett.* **30**, pp. 861-863 (2009). (Cited: 4) (SCI IF: 2.607)
14. Tsan-Wen Lu*, Yi-Hua Hsiao, Wei-De Ho, and **Po-Tsung Lee**, "Photonic crystal hetero-slab-edge microcavity with high quality factor surface mode for index sensing," *Appl. Phys. Lett.* **94**, 141110 (2009). (Cited: 9) (SCI IF: 3.854)
15. Albert Chin*, Ming-Feng Chang, S. H. Lin, W. B. Chen, **Po-Tsung Lee**, F. S. Yeh, C. C. Liao, M. F. Li, N. C. Su and S. J. Wang, "Flat Band Voltage Control on Low V_t Metal-Gate/High-κ CMOSFETs with small EOT," *Microelectron. Eng.* **86**, pp. 1728-1732 (2009). (SCI IF: 1.537)
16. Hsiao-Wen Zan*, Cheng-Wei Chou, Chung-Hwa Wang, Ho-Tsung Song, Jenn-Chang Hwang, and **Po-Tsung Lee**, "Carbon Attachment on the Aluminum Nitride Gate Dielectric Pentacene Based Organic Thin Film Transistors," *J. Appl. Phys.* **105**, 063718 (2009). (Cited: 1) (SCI IF: 2.201)
17. Tsan-Wen Lu* and **Po-Tsung Lee**, "Ultra-high sensitivity optical stress sensor based on double-layered photonic crystal microcavity," *Opt. Express* **17**, pp. 1518-1526 (2009). (Cited: 10) (SCI IF: 3.935)
18. Ming-Feng Chang, **Po-Tsung Lee**, S. P. McAlister, and Albert Chin*, "Small Sub-threshold-Swing and Low-Voltage, Flexible Organic Thin Film Transistors which use HfLaO as the Gate Dielectric," *IEEE Electron. Device Lett.* **30**, pp. 133-135 (2009). (Cited: 13) (SCI IF: 2.607)

(II) International Invited Talks

1. "One- and Two-Dimensional Photonic Crystal Devices for Nanolaser and Optical Sensor Applications," 2011 International Photonics Conference (*IPC*) (2011).
2. "Nano-fabrication of photonic crystal devices for nanolaser and optical sensor applications," 2011 Workshop on High-Aspect-Ratio Micro-Structure Technology (*HARMST*) (2011).
3. "Photonic Crystal Lasers for Optical Sensing Applications," 第一屆海峽兩岸奈米光子學研討會 (2011).
4. "Photonic Crystal Hetero-Slab-Edge Microcavity with High Quality Factor Surface Mode for Index Sensing," 第三屆兩岸光學研討會 (2009).

(III) International Conference Papers

1. **Po-Tsung Lee*** and Tsan-Wen Lu, "One- and Two-Dimensional Photonic Crystal Devices for Nanolasers and Optical Sensors," *IPC'11*, Tainan, Taiwan (2011). (Invited)
2. Kuang-Yang Kuo*, Shu-Wei Hsu, Wen-Ling Chuang, and **Po-Tsung Lee**, "Study on the nano-crystalline Si embedded ZnO thin films for solar cell application," 729-D, 37th *IEEE PVSC*, Seattle, Washington, USA (2011).
3. Chia-Yang Tsai*, Shao-Ping Lu, Jyun-Wei Lin, and **Po-Tsung Lee**, "High sensitivity plasmonic index sensor using slab-like gold nanoring array," JTul66, *IEEE/OSA CLEO/QELS'11*, Baltimore, Maryland, USA (2011).
4. Shao-Pin Lu*, Pin-Tso Lin, and **Po-Tsung Lee**, "All-Optical Controllable Transport of Subwavelength Sized Particles on a Tapered Photonic Crystal Waveguide," OPT1-O-17, *OPT'10*, Tainan, Taiwan (2010).
5. Wen-Ling Chuang*, Shu-Wei Hsu, Kuang-Yang Kuo, and **Po-Tsung Lee**, "Optical and Electrical Characteristics of Nano-Crystalline Si Embedded in the ZnO Matrix," OPT9-P-098, *OPT'10*, Tainan, Taiwan (2010).
6. Jyun-Wei Lin*, Chia-Yang Tsai, and **Po-Tsung Lee**, "One-dimensional composite-gradual photonic crystal with broadband omni-directional reflection," OPT5-O-31, *OPT'10*, Tainan, Taiwan (2010).
7. Li-Hsun Chiu*, Tsan-Wen Lu, Shao-Ping Lu, and **Po-Tsung Lee**, "Ultra-compact one-dimensional photonic crystal nanobeam laser," OPT1-O-02, *OPT'10*, Tainan, Taiwan (2010). (Best Student Oral Paper Award)
8. Shu-Wei Hsu*, Wen-Ling Chuang, Kuang-Yang Kuo, and **Po-Tsung Lee**, "Morphologic effect on the formation of nano-crystalline Si embedded in the ZnO matrix," OPT9-O-15, *OPT'10*, Tainan, Taiwan (2010).
9. Pin-Tso Lin*, Tsan-Wen Lu, and **Po-Tsung Lee**, "All-optical Controlled-transport Of Nanoparticles On Wedge-shaped Photonic Crystal Waveguides," IWB4, *OSA IPRSN'10*, Monterey, California, USA (2010).
10. Tzu-Yueh Chang*, Chun-Lung Chang, Hsin-Yu Lee, and **Po-Tsung Lee**, "Characteristics of MIS Solar Cells Using A Sputtering SiO₂ Insulating Layer," 302-I15, *IEEE 35th PVSC*, Honolulu, Hawaii, USA (2010)
11. Tsan-Wen Lu*, Pin-Tso Lin, Kuan-Un Sio, and **Po-Tsung Lee**, "Square Lattice Photonic Crystal Point-Shifted D₀ Nanocavity with Lowest-Order Whispering-Gallery Mode," CWK5, *IEEE/OSA CLEO/QELS'10*, San Jose, California, USA (2010).
12. Yi-Heng Tsai, Yi-Shian Lin, Tzu-Yueh Chang*, and **Po-Tsung Lee**, "Annealing Condition Dependent Room Temperature PL of Si Nano-crystals Thin Film," T10.32, *2010 MRS Spring Meeting*, San Francisco, California, USA (2010).
13. You-Wei Cheng, Tzu-Yueh Chang*, and **Po-Tsung Lee**, "Characteristics of Organic Memory Using Metal Oxide Nano-clusters," G17.3, *2010 MRS Spring Meeting*, San Francisco, California, USA (2010).
14. Yi-Hua Hsiao, Tsan-Wen Lu*, Wei-De Ho, and **Po-Tsung Lee**, "High-Q Photonic Crystal Hetero-Slab-Edge Microcavity Laser for Index Sensing," CTuDD4, *IEEE/OSA CLEO/QELS'09*, Baltimore, Maryland, USA (2009).
15. Wei-De Ho*, Yi-Hua Hsiao, Tsan-Wen Lu, and **Po-Tsung Lee**, "Thermal Properties of Post-Size Controlled 12-Fold Quasi-Photonic Crystal Microcavity for Electrically-Driving," CFE4, *IEEE/OSA CLEO/QELS'09*, Baltimore, Maryland, USA (2009).

(IV) Domestic Journal Papers

1. **Po-Tsung Lee*** (李柏聰) and Tsan-Wen Lu (盧贊文) "從元件有效面積縮小化談近期一維光子晶體奈米樑共振腔元件的發展與應用," *真空科技*, 24 卷 1 期, 頁 84-93 (2011). (Invited)
2. Tsan-Wen Lu* (盧贊文) and **Po-Tsung Lee** (李柏聰) "正方晶格光子晶體奈米共振腔雷射及其光學感測應用," *中華民國光學工程學會季刊*, 第 111 期 (99.7), 頁 11-21 (2010). (Invited)